Engineering Hard Ferrite Composites by Combining Nanostructuring and Al^{3+} Substitution: from Nano to Dense Bulk Magnets

Pierfrancesco Maltoni[*,↓,1], *Gianni Barucca*[2], *Bogdan Rutkowski*[3], *Sergey A. Ivanov*[1], *Nader Yaacoub*[4], *Anastasiia Mikheenkova*[5], *Gustav Ek*[5], *Mirva Eriksson*[6], *Bjarne Almqvist*[7], *Marianna Vasilakaki*[8], *Gaspare Varvaro*[9], *Tapati Sarkar*[1], *José A. De Toro*[10], *Kalliopi Trohidou*[8], *Davide Peddis**[9,11], *Roland Mathieu**[1]

1. Department of Materials Science and Engineering, Uppsala University, Box 35, Uppsala, 751 03 Sweden
2. Dipartimento di Scienze e Ingegneria della Materia dell'Ambiente ed Urbanistica – SIMAU, Università Politecnica delle Marche, Ancona 60131, Italy
3. AGH University of Krakow, Faculty of Metals Engineering and Industrial Computer Science, Al. A. Mickiewicza 30, Kraków 30-059, Poland
4. Institut des Molécules et Materiaux du Mans, CNRS UMR-6283, Le Mans Université, F-72085 Le Mans, France
5. Department of Chemistry - Ångström Laboratory, Structural Chemistry, Uppsala University, Uppsala, 752 36 Sweden
6. Arrhenius Laboratory, Department of Materials and Environmental Chemistry, Stockholm University, S-10691, Stockholm, Sweden
7. Department of Earth Sciences, Geophysics, Uppsala University, Villavägen 16, Uppsala, 751 03 Sweden
8. Institute of Nanoscience and Nanotechnology, NCSR "Demokritos", 153 10 Agia Paraskevi, Attiki, Greece
9. Consiglio Nazionale delle Ricerche, Istituto di Strttura della Materia, nM^2-lab, Monterotondo Scalo (RM), 00015 Italy
10. Instituto Regional de Investigación Científica Aplicada (IRICA) and Departamento de Física Aplicada, Universidad de Castilla-La Mancha, Ciudad Real, 13071 Spain
11. Dipartimento di Chimica e Chimica Industriale & INSTM,nM^2-Lab, Università degli Studi di, Genova, Via Dodecaneso 31, Genova, 1–16146 Italy

[↓]*Present Address*: Dipartimento di Chimica e Chimica Industriale & INSTM,nM2-Lab, Università degli Studi di, Genova, Via Dodecaneso 31, Genova, 1–16146 Italy; Consiglio Nazionale delle Ricerche, Istituto di Strttura della Materia, nM^2-lab, Monterotondo Scalo (RM), 00015 Italy

Keywords: ferrites, super-exchange coupling, interfaces, nanoparticles, permanent magnet

ABSTRACT

We have investigated the bottom-up sol-gel synthesis of nanocomposite powders comprising two magnetic phases (hexagonal Sr ferrite and spinel Co ferrite) in order to outline a strategy to obtain permanent magnets with large coercivities via low-cost and scalable syntheses. The correlation between morphological, structural and macroscopic magnetic properties of Al-substituted $SrFe_{12}O_{19}$ and $SrFe_{12}O_{19}/CoFe_2O_4$ nanocomposites was analyzed in detail. The hysteretic behavior can be tuned by cation substitution and/or modulation of the super-exchange coupling at the interface of the constituting phases. The magnetic data, supported by Monte Carlo simulations, indicates enhanced magnetic coupling within the composite: this observation underscores the significance of soft crystallite size and epitaxial growth quality at the interface as key factors influencing super-exchange coupling strength,

ranging from fully coupled to essentially decoupled composites. Bulk magnets with high density were manufactured by compacting these nanostructured phases using spark plasma sintering, without an applied magnetic field. Consolidation of powders significantly impacted magnetic properties, by increasing remanent magnetization and decreasing coercivity due to enhanced super-exchange coupling. The presence of two phases hindered reciprocal growth, influencing coercivity differently in various compositions. Overall, the compaction enhanced magnet performance through improved particle alignment and super-exchange coupling, offering the potential for optimized magnet design.

1. Introduction

Permanent magnets (PM) play a significant role in a multitude of energy-related technological applications, as building blocks of electromotors, generators, wind turbines, hydropower, and magnetocaloric refrigeration [1,2]. The transition from fossil to sustainable energy thus implies an ever-increasing demand for permanent magnets. In the search for environment-friendly materials, ferrites have regained attention in recent years, in particular due to the possibility of nanostructuring as a strategy to enhance the magnetic properties and, in turn, increase the energy product, $(BH)_{MAX}$ [3–6]. Among these iron-containing magnetic oxides, which account for the majority of the PM market by weight (~85 wt%) [7,8], $SrFe_{12}O_{19}$ (SFO) exhibits a large coercivity (due to its large magnetocrystalline anisotropy), high chemical stability, availability of raw material powders, low cost, high Curie temperature, and low eddy current losses [9,10]. Commercial standard ferrite magnets, such as the Hitachi Metals NMF-15 series, offer a high remanence induction of up to 480 mT and a maximal energy product $(BH)_{MAX}$ of 44 kJ/m³. These properties make them suitable for applications requiring strong, compact permanent magnets with good magnetic hardness and stability. Despite their moderate saturation magnetization and anisotropy, these ferrites provide a cost-effective solution for a wide range of industrial and consumer uses.

Beyond reducing the size down to the nanoscale [11], there are two main viable routes to tune the hysteretic response of such material: (i) modifying the atomic structure by strategically replacing metal cations in specific sites, (ii) combining two or more exchange coupled magnetic phases with different properties (i.e., hard, with large magnetocrystalline anisotropy, and soft, with high saturation magnetization, phases) [5,12–14]. The first strategy allows producing ferrites with coercivity values well above ~500 kA/m [15–19], typically observed for unsubstituted SFO [9,20], demonstrating the possibility to increase the coercivity by simply replacing Fe^{3+} with diamagnetic cations, such as Al^{3+}, without formation of impurity parasitic phases. However, a compromise has to be reached due to the concurrent decrease of the saturation magnetization mainly due to the replacement of Fe^{3+} ions in the spin-up sites of the ferrimagnetic SFO structure [21]. The second strategy, first discussed in the seminal work of Kneller *et al.*[12], predicts an enhancement of $(BH)_{MAX}$ when magnetically hard and soft phases are exchange coupled at the interface. This strategy has attracted huge interest from the scientific community, which resulted in several synthetic approaches to produce magnetic nanocomposites based on ferrites of different morphologies (e.g., core-shell, mixtures, nano-heterostructures) with improved magnetic properties [22–31]. The key parameters to achieve an effective coupling rely on a structurally coherent soft-hard interface and limiting the size of the soft regions below the critical limit for rigid coupling.

The subsequent manufacturing of ferrites into bulk permanent magnets is an essential step that presents some challenges to preserve the desired properties achieved by the synthetic design (i.e., nanostructure and improved magnetic properties) of the starting powder building-blocks upon sintering/compaction [32]. This process often results in grain growth (sometimes leading to the formation of multi-domain particles and, in turn, reduced coercivity) or even side reactions (like chemical diffusion or phase segregation) [33–35]. Also, the alignment of the

crystallites has to be induced during their assembly into bulk magnets in order to achieve high magnetic performances (i.e., large $(BH)_{MAX}$ values). Among the various processes successfully developed in recent years to densify ferrite permanent magnets, including compaction in a magnetic field, bonding, cold- and conventional-sintering, and additive manufacturing [36–42], spark plasma sintering (SPS) has demonstrated to be an efficient approach to fabricate highly-dense magnets (particle density, $\varphi=\rho_{SPS}/\rho_{bulk}$, above 90%) using very short times and low temperatures compared to those involved in conventional processes, as shown by Christensen *et al* [3]. Furthermore, the process was demonstrated to facilitate a self-induced crystallite alignment, resulting in a magnetic alignment and an increase of $(BH)_{MAX}$ [37]. However, the achieved values remain lower than those of commercial magnets, highlighting a gap that must be bridged for wider adoption. Achieving competitive performance requires addressing key challenges such as controlling crystallite growth, preventing impurity formation, and ensuring proper magnetic orientation during compaction. In the broader context of developing substitute magnets with $(BH)_{MAX}$ values between 40-200 kJ/m³ for applications that do not require the highest performance, strategies such as coupling nanomaterials with different magnetic properties in composites could significantly improve the performance of known materials. The potential of SPS technique to produce magnets from super-exchange coupled composites as building blocks has been rarely explored [43,44]. Thus, further exploration and optimization of nanoparticle consolidation techniques, alongside innovative composite strategies, are essential to developing competitive permanent magnets.

This work presents the application of the SPS technique in a series of super-exchange coupled nanocomposites (made of $SrFe_{12-x}Al_xO_{19}/CoFe_{2-y}Al_yO_4$ 90/10 wt%) obtained from a easily scalable bottom-up sol-gel self-combustion synthesis. The weight fraction was chosen to prevent the growth of the softer phase and in turn maximize the magnetic coupling at the interface [45]. The synthetic design of the composites was optimized to firstly tune the hardness of the SFO phase via Al^{3+} substitution, and secondly to modify the synthesis approach to achieve a different morphology (i.e., epitaxial growth at the interface), composition (thus controlling the hard/soft character of the individual phases) and the crystallite size, according to our previous studies.

The relationship between nanostructure, interface between magnetic phases, and magnetic properties of the building blocks was investigated by a number of complementary techniques, including synchrotron X-ray powder diffraction (XRPD), transmission electron microscopy (TEM), scanning transmission electron microscopy (STEM), energy dispersive X-ray spectroscopy (EDX), and magnetometry. The primary objective is to provide insight on the synthetic strategies offered by the sol-gel process in the preparation of super-exchange coupled nanocomposites, and the control over size, morphology and composition that can be achieved. Finally, the potential of SPS-processed bulk magnets is discussed.

2. Experimental Section/Methods

2.1. Synthesis of $SrFe_{12-x}Al_xO_{19}$ nanocrystallites

The hexagonal $SrFe_{12-x}Al_xO_{19}$ with x being the Al^{3+} content (x=1, 1.4, 2, 2.4) were prepared by a sol–gel combustion process[46]. Briefly, $Fe(NO_3)_3 \cdot 9H_2O$, $Al(NO_3)_3 \cdot 9H_2O$ and $Sr(NO_3)_2$ (Sigma-Aldrich) were dissolved in deionized water to give a Fe^{3+} concentration of 0.2 M, with a $(Fe^{3+}+Al^{3+})/Sr^{2+}$ molar ratio equal to 11 (Sr^{2+} excess). Then a 1 M citric acid aqueous dispersion was added. The pH of the solution was adjusted to 7 adding dropwise NH_3 (30%) (Sigma-Aldrich). Next, it was heated on a hot plate to 80 °C to form a gel, thanks to the chelating action of the citric acid. After the entire solution was converted to a dry gel, the temperature was rapidly increased to 300 °C inducing a flameless self-combustion. The obtained dry powders were ground and annealed at 1100 °C for 6 h with a ramp of 5 °C

min^{-1} under air. We will refer to this series as SFAO_x. Two additional unsubstituted $SrFe_{12}O_{19}$ samples were prepared for comparison in different annealing conditions (1100 °C for 6 h, SFO@1100, and 950 °C for 3 h, SFO@950).

2.2. Synthesis Strategies for nanocomposites

Four nanocomposites with the same fixed $CoFe_2O_4$ weight fraction (wt%) were prepared following three different synthetic strategies:

1. Two nanocomposites comprising the $SrFe_{12}O_{19}$/ $CoFe_2O_4$ (SFO/CFO) 90/10 wt% and the corresponding Al^{3+} substituted $SrFe_{10.3}Al_{1.7}O_{19}/CoFe_{1.7}Al_{0.3}O_4$. Hereafter we will refer to these as NC_1 and NC, respectively. Briefly, the composites were prepared by a sol-gel synthesis using Fe, Sr, Al and Co nitrates in an appropriate ratio, and citric acid as chelating agent [46]; the post-synthesis powder-like products were subsequently annealed at 950 °C for 3 h and 1100 °C for 6 h, respectively, with a ramp of 5 °C/min under air.
2. A $SrFe_{10}Al_2O_{19}/CoFe_2O_4$ nanocomposite obtained by a seed-mediated synthesis designed by the authors [47] (NC_SM); preformed 9 nm NPs of CFO synthesized by thermal decomposition [48] were inserted in the reaction environment of a typical sol-gel synthesis used in (1): after dissolving the precursors of SFO, the seeds NPs, previously stabilized in water, are added to the dispersion. The pH is adjusted to 10 to achieve colloidal stability (i.e., strong electrostatic repulsion provided by the coating), and, in turn, allowed us to control the NPs agglomeration in the $SrFe_{10}Al_2O_{19}$ matrix limiting the crystallites growth after annealing (which was carried out in the same conditions as for NC).
3. A $SrFe_{10}Al_2O_{19}/CoFe_2O_4$ nanocomposite prepared by physically mixing CFO particles (~20 nm in size, obtained by sol-gel synthesis) and the precursors of the desired $SrFe_{10}Al_2O_{19}$ particles (i.e. $SrCO_3$, and Al^{3+} substituted Fe_2O_3 phases, obtained after the combustion step of the sol-gel synthesis used in (1) without further annealing) in a mortar for 1h to obtain the desired final wt% of 90/10 SFO/CFO, which were then annealed in the same conditions as NC and NC_SM, necessary to form the hexagonal phase (NC_MIX).

2.3. Spark Plasma Sintering (SPS)

Five powder samples (SFO@950, NC_1 (SFO/CFO 90/10 wt%), SFAO_2, NC and NC_SM) were compacted and sintered into bulk magnets (SPS_SFO, SPS_NC_1, SPS_SFAO_2, SPS_NC and SPS_NC_SM) by spark plasma sintering (SPS) technique. The final disc-like pellets have a diameter of ~8 mm and a thickness of ~3 mm. Briefly, ~0.8 g of powders were inserted in a graphite die, the inside was protected by a thin graphite paper. Uniaxial pressure of 100 MPa was applied at 400^{O}C and heating rate of 100^{O}C/min from 600^{O}C was applied until sintering temperature of 900^{O}C with holding time of 2 min in SPS 825, Dr Sinter, Fuji Electronics; detailed sintering profile is shown in Section 1 of SI. To evaluate the maximum energy product, $(BH)_{MAX}$, the effective (internal) magnetic field was considered by applying the demagnetizing field correction of the disc using the model reported by P.S. Normile et al. [49]. An example of a SPS-densified magnet (with 90% of the bulk density, ρ_{bulk}=5100 kg/m^3, i.e. $\varphi=\rho_{SPS}/\rho_{bulk}$=0.9) obtained from NC_1 powder and labelled SPS_NC_1 is shown in **Figure S10**. Note that no magnetic field was applied during the SPS sintering process, which reaches T ~1173K, a temperature above the Curie points of either phase in the composite[50].

2.4. Characterization

Transmission electron microscopy (TEM) studies were carried out on the powder samples in a Philips CM200 microscope operating at 200 kV and equipped with a LaB_6 filament. Scanning-transmission electron microscopy (STEM) analysis was carried out with a probe Cs-corrected FEI Titan3 G2 60-300 STEM equipped with ChemiSTEM technology (X-FEG field emission gun and Super-X EDX detector system) developed at FEI (FEI application note AN002707-

2010) for energy dispersive X-ray (EDX) microanalysis. Samples for TEM and STEM observations were prepared by dispersing a small amount of the sample, in form of a powder, in ethylic alcohol and the solution was submitted to ultrasonic agitation for one minute. A drop of the suspension was then deposited on a commercial TEM grid covered with a holed thin carbon film, and the grid was kept in air until complete ethanol evaporation. The atomic models of the SFO and CFO phases were created by using Rhodius software from Universidad de Cadiz (Pérez-Omil, J.A. TEM-UCA software (2018). University of Cádiz. http://www.uca.es/tem-uca).[51]
Structural characterization of the powder samples (SFAO_x, NC, NC_SM and NC_MIX) by synchrotron radiation X-ray powder diffraction at the P02.1 beamline at DESY in Hamburg, Germany. The wavelength was determined as 0.20717 Å by using a LaB_6 standard. The integrated diffractograms were refined using the Rietveld method [52], via the program FullProf (see SI for more details on the refinement).[53] The diffraction peaks were described by a modified Thompson–Cox–Hastings pseudo-Voigt function. Structural and microstructural characterization of the crushed SPS magnets was carried out by in-house Bruker D8 Advance diffractometer (solid state rapid LynxEye detector, Cu Kα radiation, Bragg–Brentano geometry, DIFFRACT plus software). In all cases, a powder diffraction pattern of a NIST LaB_6 660b standard was collected for corrections.
Elemental analysis was performed by inductively coupled plasma optical emission spectroscopy (ICP-OES) and energy dispersive X-ray (EDX) microanalysis on the selected powder samples. The morphological and compositional properties of SPS pellets were analyzed by Scanning electron Microscopy (SEM) and EDX correspondingly. The samples were polished using diamond lapping powders with different grain size (7–40 μm) before the measurements. The images presented in the work were collected on Zeiss LEO 1530 with Oxford AZtec EDS system at 5 kV acceleration voltage and 5 mm working distance. The EDX measurements were performed at 20 kV acceleration voltage and 8.5 mm working distance.
Isothermal field-dependent magnetization loops were recorded at 300K of the powder samples (using a Quantum Design MPMS SQUID magnetometer), by sweeping the field in the −5T to +5T range, and the obtained magnetization values were normalized by the weight of powders present in the sample and expressed in Am^2kg^{-1}. To get information about the irreversible processes, direct current demagnetization (DCD) remanence curves were measured by applying a progressively higher DC reverse field to a sample previously saturated under a field of −5T and by recording, for each step, the value of the remanent magnetization, which was then plotted as a function of the reverse field. The magnetization loops of the SPS magnets in a out-of-plane configuration was carried out using a vibrating sample magnetometer (VSM; Lake Shore VSM model 7400) operated in a field range of ±1.8 T.

2.5. Monte Carlo simulations

For the numerical study of the NC, NC_SM and NC_MIX nanocomposites, we use the Monte Carlo simulation technique with the implementation of the Metropolis algorithm[54,55]. We consider dense assemblies of hard SFO and soft CFO spherical nanoparticles with diameter *d*, and total particle concentration c= 60% at the nodes of a simple cubic lattice of characteristic length $L_x=L_y=L_z=10\alpha$. The parameter α is defined as the smallest inter-particle distance equal to the particle diameter. The hard/soft particle volume ratio is taken 90%/10% as in the experimental samples. In the NC and NC_SM samples the nanoparticles are randomly placed in the cubic lattice. In the NC_MIX sample, based on the TEM images which indicate segregation of the CFO and of SFO phases, we consider the following topology: the particles of the soft phase are clustering in the 1/8 of the space while the particles of the hard phase occupy the rest of the space (see **Figure 1**). More details can be found in SI.

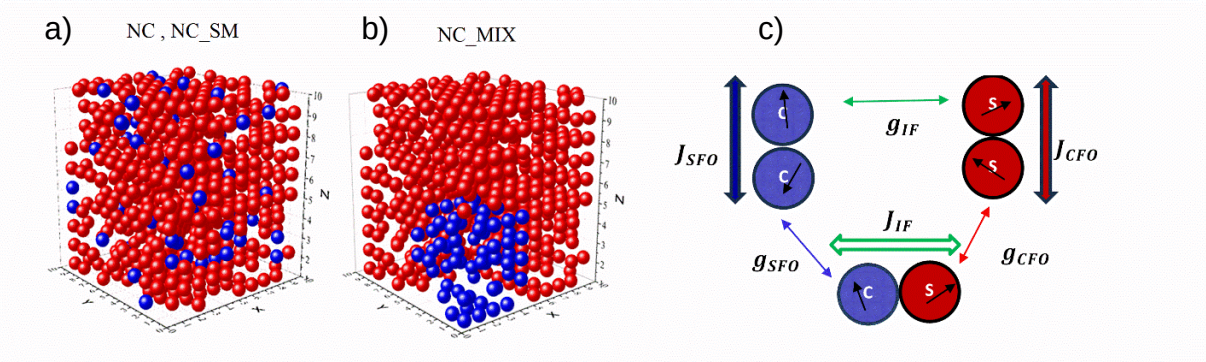

Figure 1: Schematic representation of the different topologies of the assemblies of SFO (red) and CFO (blue) nanoparticles for NC, NC_SM (a) and NC_MIX nanocomposites (b). The exchange coupling constants and the dipolar interparticle interaction strengths between the particles are depicted (c).

3. Results and Discussion

In the next sections, we will show two different strategies to tailor the magnetic response of nanocomposites: (i) by tuning the magnetic anisotropy of the magnetically hard phase (SFO) via chemical substitution with diamagnetic Al^{3+} cations, and (ii) by modifying the interfacial morphology in a set of nanocomposites (substituted with Al^{3+} and with a fixed 10 wt% CFO phase) using three different synthetic approaches.

3.1. Enhancing the magnetic anisotropy of the hard phase by Al^{3+} substitution

The Rietveld refinement of XRPD results for a set of $SrFe_{12-x}Al_xO_{19}$ (SFAO_x, with $1<x<2.4$) particles, treated at 1100 °C in air for 6 hours, confirmed that the magnetoplumbite *P6₃/mmc* spacegroup is preserved even for large x substitution (**Figure 2a**). The composition was verified by both ICP and EDX techniques as reported in **Table 1**. The high-quality data allows for excluding the presence of secondary impurities (i.e. *R-3c* of α-Fe_2O_3) and determining the accurate cationic distribution among the Fe^{3+} sites. The inclusion of Al^{3+} in the structure induces a shift of the Bragg reflections to higher q-values for increasing contents compared to the unsubstituted SFO@950 and SFO@1100 reference samples (treated at 950°C for 3 hours and 1100°C for 6 hours respectively), which show similar unit cell parameters but different crystallite size: the unit cell parameters decrease accordingly, from a=b=5.84704 Å and c=23.02855 Å (SFO@950) to 5.82075 Å and 22.83677 Å (SFAO_2.4), respectively, in agreement with previous observations for similar ferrites [18,56,57]. TEM observations show that particles have the shape of platelets (**Figure S1**). This feature is typical of Sr hexaferrites obtained by sol-gel synthesis, as also reported in previous studies [9,58,59]. The structural details are reported in **section 1.1** of **SI** (see **Figure S2**, **Table S1** and **Table S2**). As shown in **Table S1**, Al occupies mainly the octahedral 2a- and 12k-sites and to a lesser extent the bipyramidal 4e-, octahedral 4f- and tetrahedral 4f-sites. Furthermore, the relative degree of site occupancy changes with increasing Al substitution, similarly to previous structural studies[17,18]. The platelet plane size extracted from the analysis of SFAO_x images, shows a monotonical decrease for increasing x despite the annealing step being carried out in the same conditions (1100 ºC in the air) for the full set. This is accompanied by a progressive decrease of the nanocrystallite size, down to ~134 nm (size extracted along the ab-plane of the platelet by XRPD, d_{SFAO}^{hk0}) and ~128 nm (along the c-axis, d_{SFAO}^{00l}) for SFAO_2.4 (**Table 1**) In addition, we observe a large broadening of the particle size distribution for x=1 followed by a progressive

narrowing of the distribution for increasing Al^{3+} contents. The structural results confirm the decrease of crystallite size with increasing Al^{3+} content (**Figure 2b**), and the corresponding decrease of micro-strain. The presence and spatial distribution of Al atoms in the SFO platelets were investigated by STEM-EDX measurements. As representative examples, **Figures 3a, b, c** and **d** show a typical high angular annular dark field HAADF-STEM image of the SFAO_2 platelets and the corresponding EDX elemental maps. EDX analysis reveals the uniform spatial distribution of Al atoms in the platelets, without evidence of segregation and compositional inhomogeneities, despite the large content (~17at. % of metallic cations). This result agrees with the perfect correspondence between the high-resolution HAADF-STEM images of the SFAO_2 lattice and the corresponding simulated model. In more detail, **Figure 3e** shows a high-resolution HAADF-STEM image of a SFAO_2 platelet in the [100] zone axis, where Sr and Fe/Al atoms appear as white dots due to the typical Z (atomic number)-contrast. Oxygen atoms are not visible due to their low atomic number. **Figure 3f** images a model of the SFAO_2 cell obtained by the Eje-Z software [60] and in **Figure 3g** a magnified area of the image in **3e** is reported with the distribution of the atoms of the SFAO_2 cell projected in [100] direction superimposed.

Table 1. Compositional analysis (atomic ratios) from ICP and EDX, unit cell parameters (a,b,c), nanocrystallite size according to the platelet vector model (d_{SFAO}^{hk0} along ab-plane and d_{SFAO}^{00l} along the c-axis), particle size from BF-TEM (d_{TEM}), platelet ratio $R^{hk0/00l}$, strain, saturation magnetization (M_S^{5T}), reduced remanence ratio (M_R/M_S^{5T}), coercive field (H_C) and Curie temperature (T_C).

Sample	x	Fe/Al ICP; EDX	a=b; c (Å)	d_{SFAO}^{hk0}; d_{SFAO}^{00l} (nm)	d_{TEM} (nm)	$R^{hk0/00l}$	Strain	M_S^{5T} (Am^2/kg)	M_R/M_S^{5T}	H_C (kA/m)	T_C (K)
SFO@950	-	-	5.87404(2); 23.02855(9)	132(2); 104(5)	140(20)	1.5	10.0(1)	69.9(5)	0.50	463(5)	740(5)
SFO@1100	-	-	5.87347(3); 23.02414(15)	197(10); 179(8)	360(75)	1.10	-	75.3(7)	0.49	315(8)	744(7)
SFAO_1	1	10.5(2); 11.1(1)	5.85398(1); 22.94835(6)	197(8); 169(8)	288(58)	1.16	4.8(1)	50.7(6)	0.51	565(6)	688(7)
SFAO_1.4	1.4	8.3(2); 7.1(2)	5.84487(1); 22.91745(7)	191(5); 145(6)	232(50)	1.35	4.7(1)	49.7(6)	0.50	674(9)	669(6)
SFAO_2	2	4.9(1); 5.1(1)	5.83066(1); 22.87078(9)	164(3); 143(5)	178(36)	1.14	6.3(1)	35.2(5)	0.50	875(8)	634(6)
SFAO_2.4	2.4	4.3(1); 4.2(1)	5.82075(1); 22.83677(8)	134(1); 128(2)	160(30)	1.04	8.9(1)	30.4(3)	0.51	945(6)	619(6)

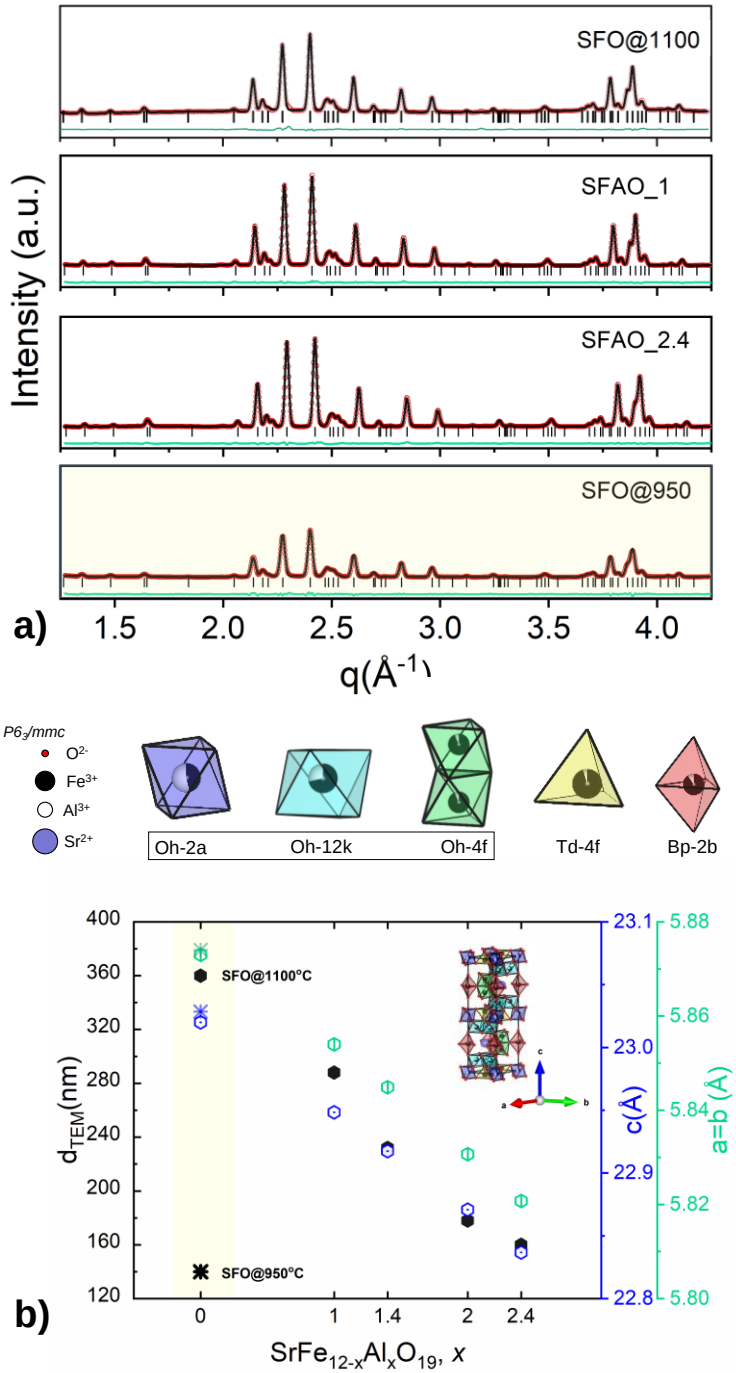

Figure 2. a) Rietveld refinement of XRPD patterns for SFO@1100, SFAO_1, SFAO_2.4 and the SFO@950 samples. The red empty markers represent the experimental data, and the black solid line is the theoretically simulated pattern; the green lines at the bottom represent the difference between the observed and simulated patterns; the ticks identify reflections for the main phase. b) Trend of particle size from TEM (d_{TEM}) and unit cell parameters from Rietveld analysis as a function of Al content (x). Above, the VESTA[61] reconstruction of the crystal structure for SFAO_2.4 and the main sites substituted by Al are reported.

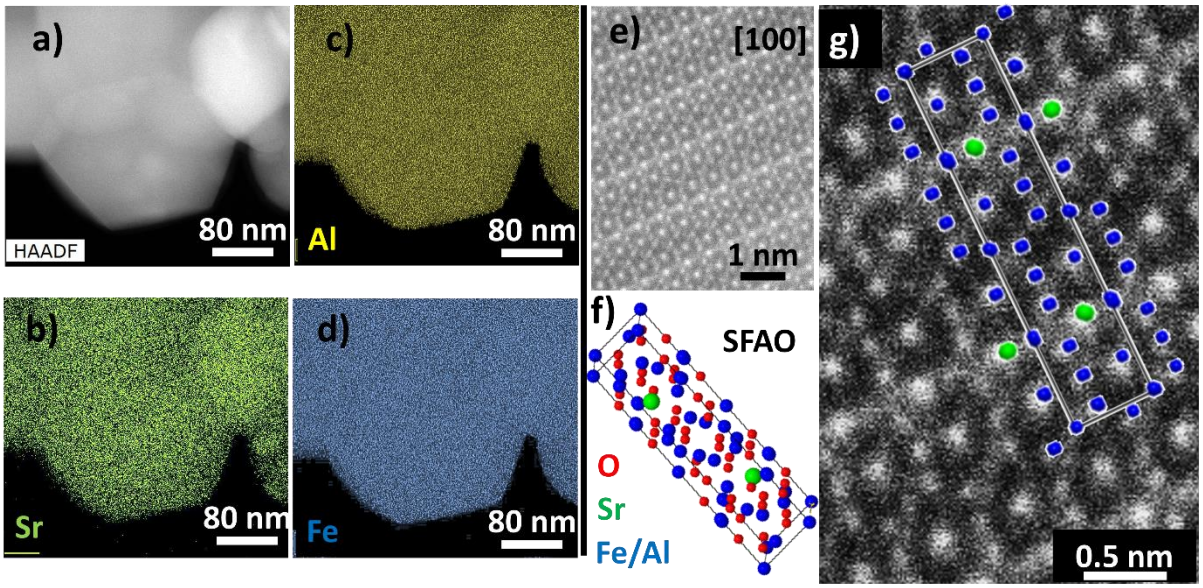

Figure 3: a) HAAD-STEM image of the SFAO_2 sample. b), c) and d) corresponding EDX maps for Sr (green), Al (yellow) and Fe (blue). e) high-resolution HAADF-STEM of SFAO in [100] zone axis. f) theoretical distribution of atoms in the SFAO_2 cell. g) magnified view of e) with the distribution of the atoms in the SFAO_2 cell projected in [100] direction superimposed (Sr atoms are green, Fe and Al are blue and oxygen atoms are not shown).

The isothermal field-dependent magnetization loops recorded at 300K (**Figure 4a**) show a reduced remanent ratio $M_R/M_S = 0.5$, where M_S is the saturation magnetization, which is typical of randomly aligned single-domain particles with uniaxial magnetic anisotropy[62]. Moreover the loops indicate a strong influence exerted by the substitution of Fe^{3+} with Al^{3+} in specific atomic sites: M_S decreases as a function of increasing Al^{3+} content, whereas the coercive field, H_C, has the opposite trend, reaching extremely large values [up to 945 kA/m ($\mu_0 H_C$ ~1.2 T)] for SFAO_2.4, doubling that of the unsubstituted SFO, among the largest reported in the literature [16,18,56]. The site-selective replacement of Fe^{3+} mainly in the 2a and then 12k octahedral sites (see **Figure 4b** and section 1.1 of **SI**) is the reason for the observed decrease in magnetization, as those are the parallel spin-up sites in the collinear ferrimagnetic structure of hexagonal M-type ferrites [57,59]. The total magnetic moment is expected to drop by 30% from SFO@1100 to SFAO_1, for the corresponding ~30% increase of Al^{3+} substitution in 2a-sites, and then by an additional 40% in SFAO_2.4, owing to the larger occupation of 2a-, 12k- and eventually bipyramidal 2b-sites. Such results are in remarkable agreement with the literature[14,63,64].

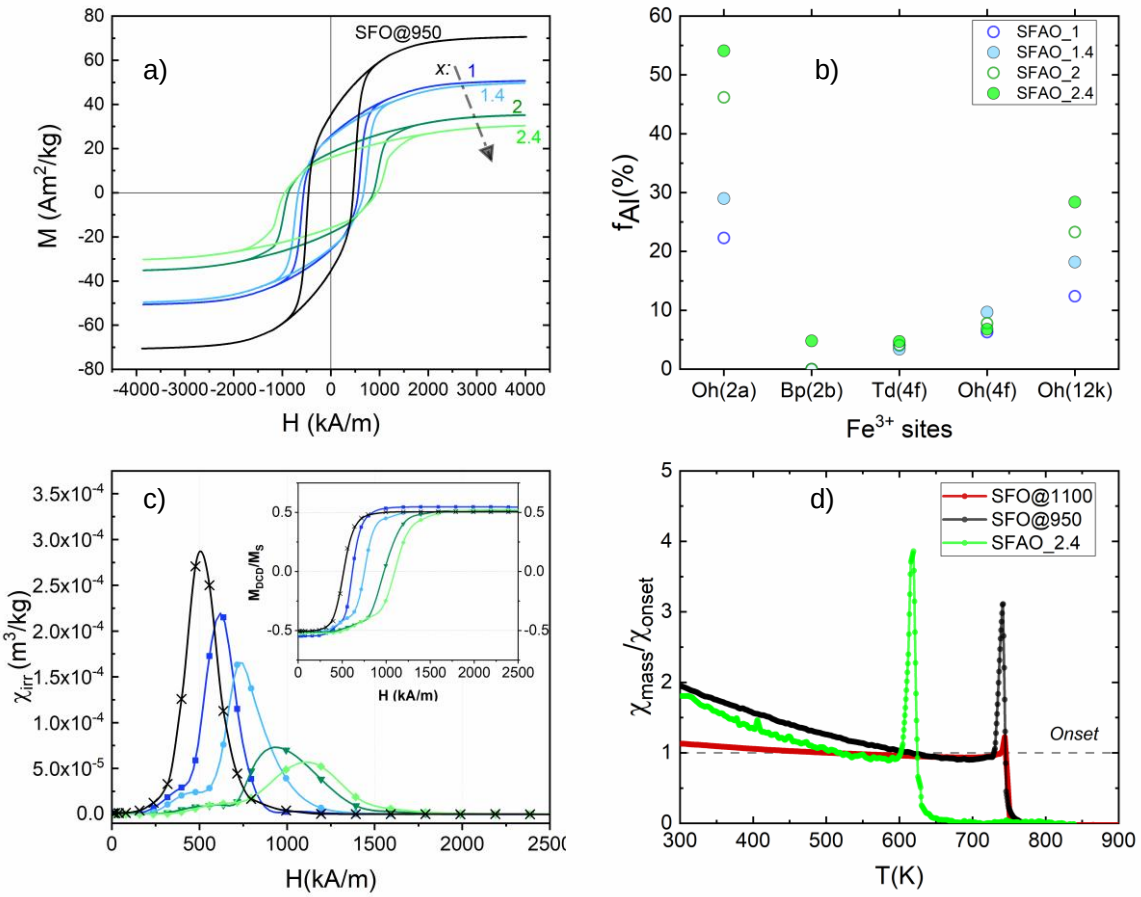

Figure 4: a) M vs H loops at 300K for SFAO_x samples. b) Fe^{3+} site occupancies from Rietveld analysis. c) χ_{irr} from first derivation with respect to H of the DCD remanent magnetization (inset). d) mass susceptibility (χ_{mass}) normalized by the susceptibility value of the peak onset (χ_{onset}) as a function of temperature (see SI).

Eventually, these results establish a strong correlation between structural observations and magnetic properties. To further study the reversal process of magnetization of the samples, remanent magnetization was recorded by DCD protocolsat 300K, and the corresponding first order differentiated curves [correlated to the switching field distributions (SFDs)] were obtained (see **Figure 4c**). The latter represents the irreversible component of the susceptibility (χ_{irr}), showing a maximum which follows the same monotonical trend as H_C for increasing amounts of Al, confirming the increase in the anisotropy field. All the Al-substituted samples show a low-field shoulder compared to the dominating high-field SFD, suggesting the presence of chemical inhomogeneities and wider particle distributions for larger Al^{3+} contents, as also observed by BF_TEM. Moreover, for the largest content of Al^{3+} the main SFD becomes more symmetric, suggesting a more uniform sample (see **Figure S3** for details). Anyhow, despite the remarkable agreement between the microstructural/morphological properties and the reversal magnetic behavior, we cannot exclude the effect of interparticle interactions and magnetocrystalline anisotropy, which are affected by the structural changes upon Al^{3+} substitution. In this regard, previous studies demonstrated that the annealing step is critical for obtaining uniformly substituted compounds to avoid inhomogeneities [18,56]. As shown in **Figure S4** and **Table S3**, a careful investigation of this step was carried out, proving that the samples in this study do not show segregation neither evident multi-phase systems (in agreement with diffraction and microscopy results).

Next, we examine the large increase in coercive field exhibited by the Al-doped samples. Considering the similar platelet-like morphology, it seems unlikely that the small variation in platelet ratio would be significant in the increase of coercivity [18,20,58,65]. More likely, the critical size for single domain particles is expected to increase upon Al^{3+} content [66]. Experimental evidence is provided by the temperature dependence of bulk mass susceptibility (χ_{mass}), shown in **Figure 4d**. The unsubstituted SFO@950 and highly substituted SFAO_2.4 samples (which have similar size and morphology), present a Hopkinson peak at the Curie temperature, T_C, (ferrimagnetic/paramagnetic transition) with different relative intensity (χ_{mass}/χ_{onset}). In contrast, for larger particle sizes (SFO@1100) we assist to a decrease in the height of the peak, indicating a change in the domain regime ascribable to a progressive transition from a single domain toward the multi-domain regime, for which the susceptibility would show a flat χ_{mass} at $T \sim T_C$ [67–69]. In fact, the height of the peak for SFAO_2.4 is higher than that of SFO@950, owing to a larger critical diameter, d_c (and thus a larger coercive field [50,70]). Note that the peak was observed for all the Al-substituted samples, showing a decrease of T_C with increasing content of Al (see **Table 1** and **Figure S5**). A simple estimation of d_c for the single-domain spin configuration may be calculated considering $d_c = 24\sqrt{AK}/N(\mu_0 M_S^2)$, where N is the geometrical shape demagnetizing factor, A the exchange-stiffness and K the magnetic anisotropy constant[50,71]. N was calculated considering the platelet-ratio (see **Table 1**) [72], A was taken to be $6x10^{-12}$ J/m as reported in Ref. [50], M_S is the experimental value and K was estimated as $K = \mu_0 H_K M_S/2$, where H_K is the anisotropy field (determined as the field at which the difference between the magnetizing and demagnetizing branches becomes ~1%)[73]. It must be pointed out that the here determined K does not correspond to the intrinsic anisotropy constant, due to extrinsic factors (such as microstructure, inhomogeneities and demagnetizing effects) that affect the properties of hard magnetic materials [74]; however, it allows comparing the variation of anisotropy for SFO@950 and SFAO_2.4 samples. Considering the evolution of K as function of the composition in **Figure S6**, the change of H_K seems correlated to the change of the M_S. The variation in d_c for the two systems with similar size and morphology (shown in **Table S4**) supports the hypothesis of the enhancement of coercivity being related to the increase in critical diameter associated with the inclusion of Al^{3+}, rather than size effects; which is instead the reason for SFO@1100 showing a decrease in H_C at about 30% compared to the SFO@950 with smaller crystallite size [58].

3.2. Synthetic design of hard-soft nanocomposites

Enhancing the coercive field of SFO by chemical composition, as shown above, is a potential way to selectively optimize the magnetic properties of the hard phase in bi-magnetic composites[5]. Next, we use this optimized SFAO as the hard component in soft-hard nanocomposites. We SM origate two synthesis methods previously adopted by the authors to design hard-soft nanostructures either with preformed particles (i.e., seed-mediated route[47], NC_SM, or growing both phases in the same reacting environment (i.e., one-pot route), NC, with a fixed 10 wt% softer phase (CFO) fraction. The CFO content was chosen according to a previous study, which established a critical limit for rigid coupling in composites with the same CFO fraction[45]. The Al^{3+} content of the hard SFAO was chosen according to the results in the previous section with x=2, showing the best compromise in terms of coercivity and saturation magnetization.

The Rietveld analysis of the data obtained by synchrotron radiation powder diffraction indicates the achievement of the desired hexagonal and spinel phases for SFAO and CFO, respectively, and a complete absence of impurities (the models are presented in section 1.2 of **SI**). When using the one-pot synthesis route a uniform distribution of Al^{3+} in both phases is observed with no selective replacement of Fe^{3+} with Al^{3+}, as expected (see **Figure 5**). Al^{3+} was

indeed found to substitute Fe^{3+} in the same sites of SFAO as previously reported, with x = 1.68 (see **Table 2**). Regarding CFO, the Rietveld model found Al^{3+} substituting the octahedral (Oh) and tetrahedral (Td) Fe^{3+}, being unlikely that Al^{3+} would replace the larger Co^{2+} ions. The elemental analysis performed by ICP considering a 10 wt% of CFO and the results from diffraction (which confirm the desired weight fractions) show a remarkable agreement (see **Table S5**). In contrast, in the NC_SM sample the use of preformed CFO NPs (whose details are reported in **Table S6**) prevents the Al^{3+} diffusion in the precursors, resulting in the desired SFAO_2/CFO composite. The extracted unit cell parameters for CFO for both NC and NC_SM confirm the random inclusion of Al^{3+} in the spinel phase of NC for both octahedral and tetrahedral sites, decreasing from ~8.37304 Å to ~8.35901 Å. Surprisingly, SFAO shows an expansion of the cell in NC_SM case. A deeper investigation reveals a different cationic distribution, namely the Al^{3+} seems to occupy a higher fraction of Tetrahedral 4f-sites, compared to SFAO_2 and NC (6.4% instead of 4.1% and 2.4%, respectively): as these sites are smaller, the results hint that the larger octahedral sites are occupied by higher contents of the larger Fe^{3+}. To confirm this hypothesis, a reference sample was prepared physically mixing preformed CFO particles and precursors of SFO and subsequently annealing the mixture to prepare the desired sample, NC_MIX, in a similar way to Ref.[45]. This approach was shown to prevent the uniform inclusion of CFO in the SFAO matrix, enabling us to isolate the role of the synthetic route. The result (occupation of 7.4% for tetrahedral 4f-site) supports the conclusion that the different annealing conditions provided by the different chemical routes (i.e., seed-mediated and mixed in contrast to one-pot) induce a different cationic redistribution in SFAO.

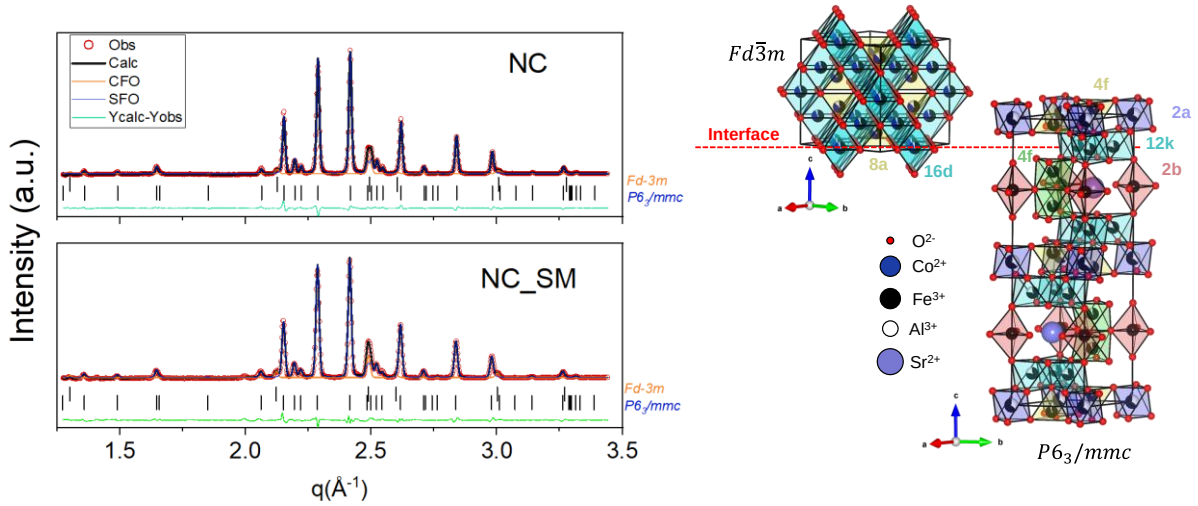

Figure 5: Rietveld analysis for NC and NC_SM patterns obtained by synchrotron-radiation powder diffraction; the red empty markers represent the experimental data, and the black solid line is the theoretically simulated pattern. The green lines at the bottom represent the difference between the observed and simulated patterns. The ticks identify reflections for the main phase and secondary spinel phase. On the right, crystallographic reconstruction of SFAO and CFO components by VESTA[61] for NC. See main text for discussion regarding the interface texture observed by electron microscopy.

Table 2. Al^{3+} content from structural analysis for SFAO and CFO fractions, CFO wt% from structural analysis, nanocrystallite size of preformed CFO particles ($d_{CFO,S}$), of CFO in the composites (d_{CFO}), of SFAO (d_{SFAO}^{hk0} and d_{SFAO}^{00l}), unit cell parameters (a,b,c), saturation magnetization (M_S^{5T}), remanence ratio (M_R/M_S^{5T}) and coercive field (H_C).

Sample	$SrFe_{12-x}Al_xO_{19}$ x=	$CoFe_{2-y}Al_yO4$ x=	CFO wt%	$d_{CFO,S}$ (nm)	d_{CFO} (nm)	d_{SFAO}^{hk0}; d_{SFAO}^{00l} (nm)	a=b; c(Å) SFAO	a=b=c (Å) CFO	M_S^{5T} (Am^2/kg)	M_R/M_S^{5T}	H_C (kA/m)
NC	1.68(5)	0.27(3)	10.1(1)	-	27(3)	122(5); 77(5)	5.83632 (1); 22.88751(8)	8.35901(1)	36.1(9)	0.55(1)	472(5)
NC_SM	2.00(5)	0	7(1)	10(2)	42(4)	144(7); 123(5);	5.84195(5); 22.91264(8)	8.37304(1)	41.9(1)	0.47(2)	470(5)
NC_MIX	2.00(5)	0	8.1(7)	21(5)	79(8)	156(8); 135(6)	5.84053(2); 22.90746(8)	8.37472(1)	41.3(7)	0.43(2)	485 (5)

To further investigate the nanostructures, STEM analysis was performed on NC and NC_SM samples. **Figure 6a** shows a HAADF-STEM image of the NC sample where SFAO_2 and CFO grains are indicated. Analyzing the interface between the two phases at high resolution, **Figure 6b**, the epitaxial growth of one phase on the other is clearly visible. By comparing the experimental image with the expected distribution of atoms obtained by the Eje-Z software in the CFO and SFAO_2 phases opportunely projected in [1-10] and [100], respectively, it is possible to identify the orientation relationships between the two phases, $(001)_{SFAO}//(111)_{CFO}$ and $[100]_{SFAO}//[1\text{-}10]_{CFO}$, (**Figure 6c** and **d**) and the atomic plane corresponding to the interface between the two phases (**Figure 6b**). The same orientation relationships were detected in other structures, such as $BaFe_{15}O_{23}/Fe_2O_3$[21,22]. The interface plane shares the octahedral Fe/Co sites of the CFO spinel structure with the Fe atoms belonging to the octahedral 12k position in the hexagonal SFO lattice, as already observed by the authors in analogous composites without Al doping [45]. The observed epitaxial growth assures a strong magnetic coupling between the two phases. In the NC_SM sample, a net visible interface between the two phases was not accessible, however, the same epitaxial growth between the two phases may not be excluded, owing to the strong magnetic coupling observed in this sample as well in the magnetic measurements.

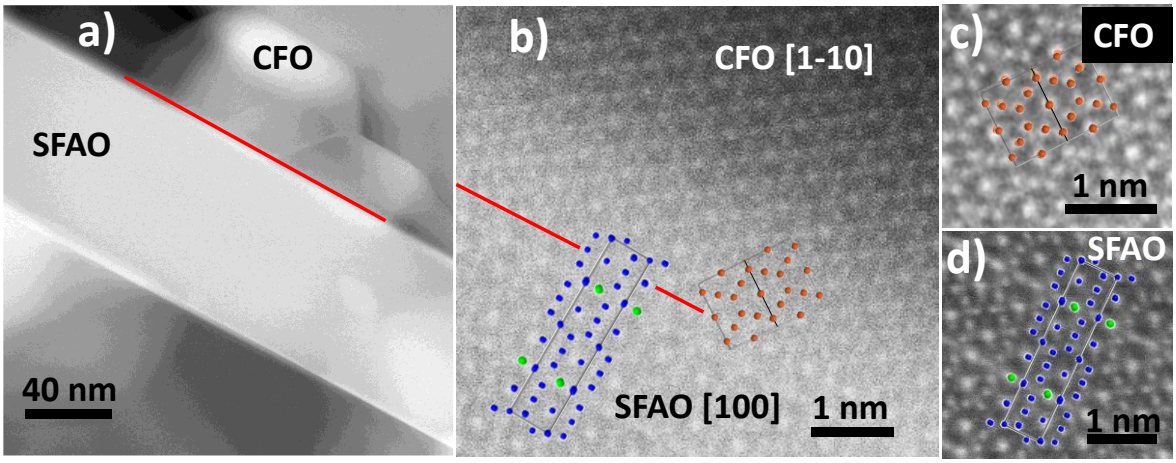

Figure 6: a) HAADF-STEM image of NC sample where the two phases are indicated. b) high-resolution HAADF-STEM image of SFAO_2/CFO interface, the atomic distributions of the two lattice cells projected in [1-10] CFO and [100] SFAO_2 are superimposed. c) and d) magnified portions of the

image in b) to better observe the correspondence between experimental data and simulated models. In the CFO model, Fe/Co atoms are drawn in orange colour, in the SFAO one, Fe/Al atoms are blue and Sr green.

The chemical composition of the nanocomposites was investigated by energy dispersive X-ray (EDX)-STEM techniques. **Figures 7a, b, c** and **d** show a typical HAADF-STEM image of the NC sample and the corresponding compositional maps for Sr, Co and Al, respectively. The CFO phase has a uniform spatial distribution in the SFAO_2 matrix, and the Al atoms appear uniformly distributed without evident segregations. The same behavior can be deduced for the NC-SM sample (**Figures 7e, f, g,** and **h**). The CFO seeds appear uniformly distributed in the SFAO_2 phase and Al atoms are present in all the SFAO_2 grains. Although the EDX measurements allowed us to highlight the presence of Al atoms and their general distribution in the two nanocomposites, it was not possible to analyze the specific presence of Al atoms in the single CFO phases, and confirm the results of XRPD measurements, because the two phases are generally overlapped.

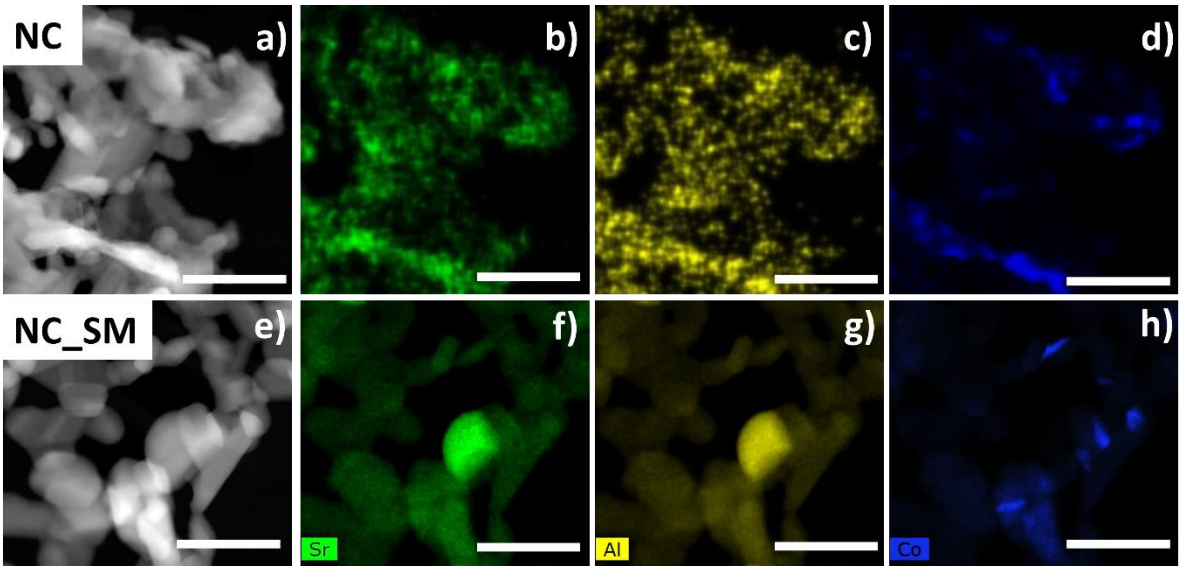

Figure 7: a) HAADF-STEM image of NC sample. b), c) and d) corresponding EDX maps for Sr (green), Al (yellow) and Co (blue). e) HAAD-STEM image of NC_SM sample. f), g) and h) corresponding EDX maps for Sr (green), Al (yellow) and Co (blue). The white bars correspond to 400 nm.

3.3. From super-exchange coupling to decoupling

Field-dependent magnetization loops were measured at 300K for NC, NC_SM and NC_MIX and are plotted in **Figure 8a**. The resulting coercivities reported in **Table 2** are lower than those of the corresponding single phases (**Table 1**) of ~40%, while the magnetization increases as a result of the coupling with CFO phase. Interestingly, despite the different Al^{3+} at. % in the SFAO phase of the composites, the coercive field of the whole set is very similar, while the trend of M_S can be simply explained as the result of larger CFO crystallite sizes for NC_SM and NC_MIX, which enhances the overall magnetization of those composites (see values reported in **Table 2**). In contrast, the expected larger magnetization due to the smaller Al content in SFAO is balanced by the lower magnetization expected for CFO due to the smaller size of the particles in NC compared to those in the other composites. Interestingly, the Al^{3+} content should yield a lower M_S in CFO, as shown in the **Figure S8** for individual samples and in the literature for particles with similar composition and lattice parameters[75,76] presumably due to the preferential substitution of Fe^{3+} in octahedral sites. However, our analysis shows that

both sites are similarly affected, revealing an effect due to the annealing step in the composite. The observed simultaneous replacement of both octahedral and tetrahedral sites, as estimated by Rietveld analysis, so that Al%(octahedral)~6.7% and Al%(tetrahedral) = 13.8%, suggests that the annealing treatment causes Al^{3+} to metastably occupy the Fe^{3+} tetrahedral site, being smaller than the Fe^{3+} octahedral site, even if Al^{3+} prefers an octahedral coordination[77]. Therefore, the differences in magnetization between the composites are unambiguously attributed to the different crystallite size of the CFO fraction and follow its evolution.

The NC_MIX loop exhibits a double-loop (also known as constricted or "hummingbird") due to the difference in coercivity of the two constituent (and segregated) phases as a result of the decoupling between the two phases leading to a deterioration of the magnetic properties[45]. This shape is much less evident for NC_SM and NC samples. Such differences were investigated by the DCD protocol to explore the independent switching of the magnetization reversal for the two phases, as shown by the SFDs in **Figure 8b**. Here, the reversal of CFO and SFAO_2 components is clearly visible for NC_MIX, while it starts becoming more uniform from NC_SM to NC. If we increase the CFO wt% to just 20%, this becomes much more evident, as the CFO component is clearly reversing independently from the harder phase (inset of **Figure 8b**). As shown in **Table 2**, moving in the direction NC_MIX, NC_SM to NC, not only the nanocrystallite size of the lower anisotropy phase is decreasing from 79(8), 42(4) to 27(3) nm, respectively, but the number of interfaces between SFAO and CFO is increasing, together with the presence of the epitaxial growth between the two phases in NC, which implies a larger degree of super-exchange coupling between the two phases [45]. The moderate increase of M_R/M_S for NC (assuming to have randomly oriented particles) above 0.5 also suggests the stronger magnetic coupling in such composite[31,78]. The findings have identified the size of the soft crystallites and the quality of the interface epitaxial growth as the two main parameters determining the strength of the super-exchange coupling, from fully coupled to essentially decoupled composites [45,79,80].

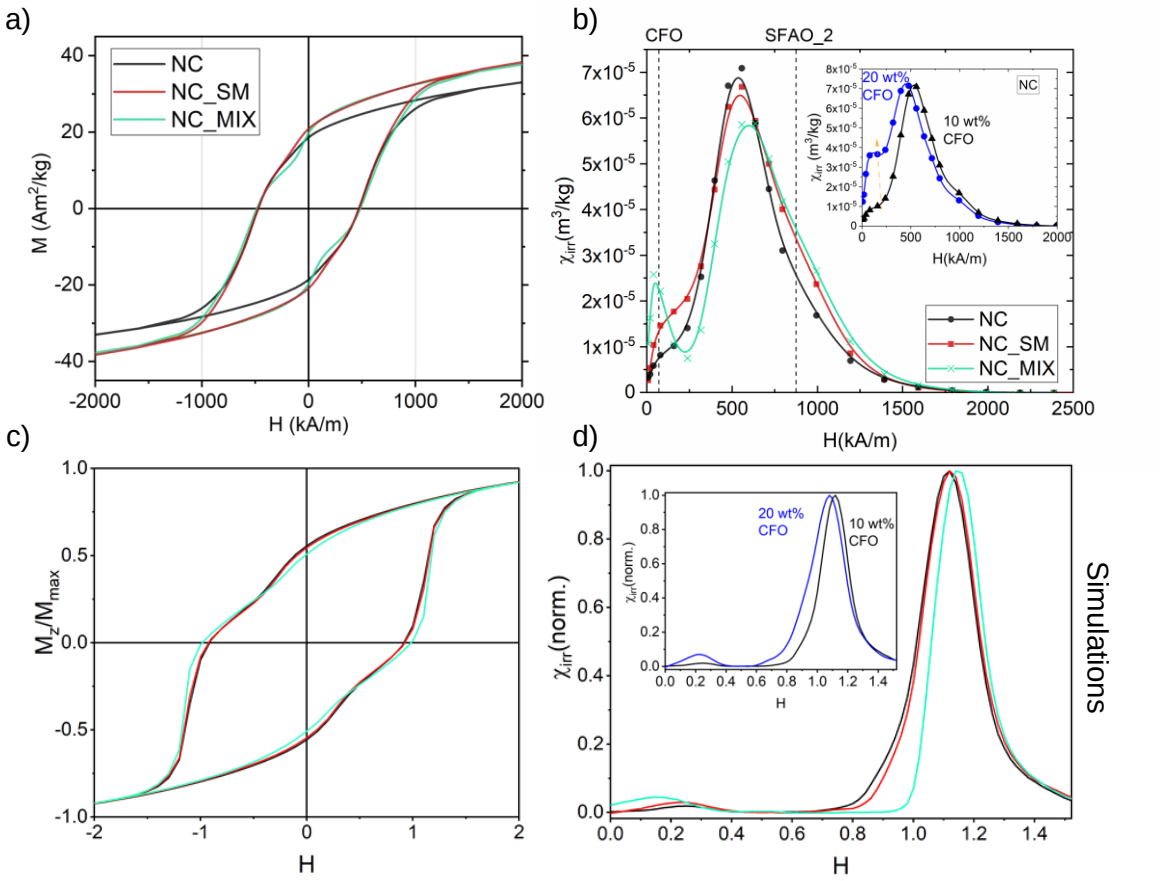

Figure 8: a) Hysteresis curves at 300K for NC, NC_SM and NC_MIX. b) χ_{irr} vs reverse field extracted from the corresponding DCD curves. The dashed lines refer to the switching field of SFAO_2 and CFO. In the inset, SFDs at 300K for the nanocomposites obtained from one-pot synthesis with 10wt.% and 20wt.% of CFO. Below, Monte Carlo simulations (in reduced units) of (a) the hysteresis loops and (b) the normalized field derivative of the DCD remanent magnetization for the corresponding nanocomposites at 300 K.

Monte Carlo simulations of the hysteresis loops for the NC, NC_SM and NC_MIX assemblies are plotted in **Figure 8c.** The results show that the super-exchange coupling between the CFO and the SFO phase plays a dominant role in the observed magnetic behaviour. Moving from NC to NC_SM and NC_MIX, the decrease of the size of the exchange coupling constant j_{IF} produces the decrease of the M_R/M_S ratio from 0.56 to 0.54 and 0.51 respectively, and the increase of the coercive field from 0.91 to 0.92 and 0.98 respectively. Interestingly, the gradual decrease of the super-exchange coupling constant affects the shape of the loop, which exhibits an increasing low-field kink in the demagnetizing curve because of the gradual decoupling of the two magnetic phases. In **Figure 8d**, the calculated normalised field derivatives of the DCD remanent magnetization (dM_{DCD}/dH) as a function of the reversed field for NC, NC_SM and NC_MIX assemblies are presented. In the case of NC_MIX, the shifting of the CFO and SFO switching fields towards lower and higher field values respectively and the increased height of the low field peak in comparison with the other nanocomposites confirms the enhancement of the non-uniform reversal of the CFO and SFO components, as j_{IF} decreases as we discussed above. Furthermore, the increase of the CFO particle concentration in super-exchange coupled NC samples from 10% to 20% and the decrease of the SFO particle concentration from 90% to 80% enhances the independent rotation of the CFO particles over the SFO particles.

3.4. SPS compaction

The potential for permanent magnets of nanocomposites based on $SrFe_{12}O_{19}/CoFe_2O_4$ nanocrystallites was recently investigated in depth [45], by compacting such powder into disc-like pellets via spark plasma sintering (SPS) (the process is described in **Figure S9**). A simple computational study (see section 2.2 of **SI**)[81,82], reveals that a fully packed magnet made with aligned particles, a maximum $(BH)_{MAX}$ = 40 kJ/m^3 can in principle be obtained for such composite, thus possibly competing with the commercial grade limit (~40 kJ/m^3) for ferrites[83,84].

Powders of NC and NC_SM were consolidated by SPS, resulting in disc-like pellets (hereafter referred to as SPS_NC and SPS_NC_SM, respectively). The calculated φ from the mass and volume of the discs and the bulk density are very high (92% and 88%, respectively, as shown in **Table 3**). The single-phase SFAO_2 was compacted into SPS_SFAO_2 as reference. From Rietveld analysis, the size of CFO remains similar to that of the initial powders, while that of SFAO increases, particularly for SPS_NC_SM (**Table 3**). The agreement of the structural model to the data also suggests that the cationic distribution was not affected by the treatment (see section 3 of **SI**). However as seen in **Figures 9a** and **b**, it is evident that this step largely affects the magnetic properties of the bulk magnets. The increase of M_S can be interpreted based on the particles' growth due to the sintering process [3,85]; nonetheless, the slight decrease of H_C for SPS_NC (~1%) compared to the initial powders confirms our hypothesis that the presence of two homogeneously distributed phases prevents the reciprocal growth, as demonstrated in previous studies , in contrast to the larger decrease (~25%) for SPS_NC_SM. The increase of M_R/M_S hints at the efficient compaction of the crystallites along the oop direction with respect to the disc[3,22]. However, the morphological properties of the starting particles that were already annealed for long times and at high temperatures, do not permit their complete orientation. To study in detail, in **Figures 9c** and **d** we have plotted the calculated hysteresis loops for the uncompacted NC and NC_SM samples (black lines) and we compare them with the results for the SPS compaction case (blue lines). In the Monte Carlo simulations, a small fraction of the anisotropy axes of SFO particles (~5%) was considered oriented along the field direction, to account for the alignment induced by the SPS process. We point out that the alignment induced by the SPS compaction was reported also in other recent studies of ferrites [3,4], as the consequence of rapid heating and uniform uniaxial pressure on plate-like particles. The simulations show that the increase in the exchange coupling strength among all the particles in the compacted samples is a result of the compaction process, which decrease the coercivity of the system and increase the remanent magnetization, owing to the coherent rotation of the spins. The effect is stronger in the case of SPS_NC_SM sample in which the exchange coupling strength is considered five times higher than that of SPS_NC sample because of the thinner sample's morphology (see section 4.1 of SI).

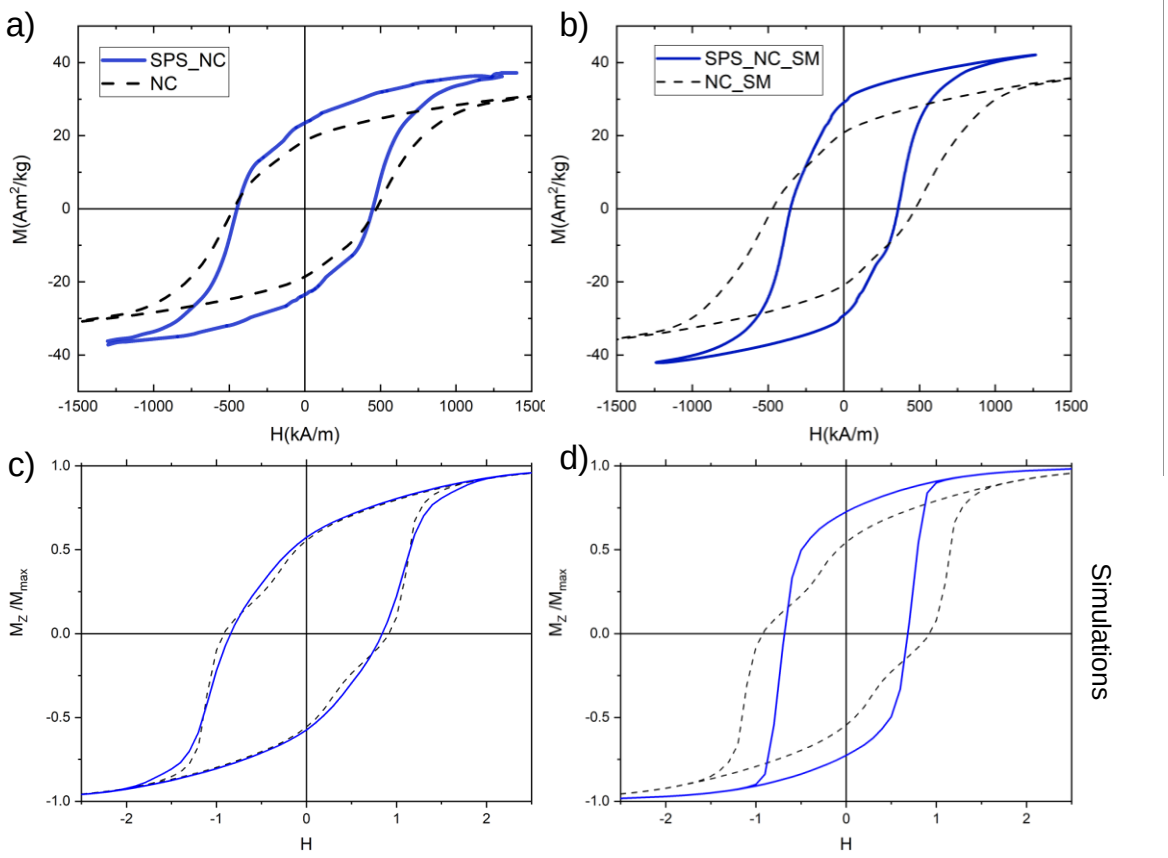

Figure 9. a) M vs H loops at 300K in the out-of-plane (oop) direction of the disc (i.e., the same corresponding to the applied uniaxial pressure during the process) for starting NC and NC_SM powders and SPS pellets (corrected for demagnetizing effects, see also Figure S13). Below, Monte Carlo simulations (in reduced units) of the hysteresis loops for the a) SPS_NC and b) SPS_NC_SM nanocomposites (blue line) and the corresponding uncompacted samples (black line) at 300 K.

Table 3. Maximum energy product, $(BH)_{MAX}$, demagnetizing factors (total $N_{P,z}$ and geometrical N_z), packing fraction ($\varphi=\rho_{sps}/\rho_{bulk}$), nanocrystallite size from XRPD analysis (d_{CFO}, d^{hk0}_{SFAO}, d^{00l}_{SFAO}), remanent magnetization (M_R), residual magnetic flux (B_R), and coercive field (H_C) for starting powders and pellets.

sample	$(BH)_{MAX}$ (kJ/m^3)	$N_{P,z}$	N_z	φ (%)	d_{CFO} (nm)	d^{hk0}_{SFAO}; d^{00l}_{SFAO} (nm)	M_R (Am^2/kg)	B_R (T)	M_R/M_S	H_C (kA/m)
SPS_SFAO_2	2.9(1)	0.66	0.68	94	-	173(8); 139(7)	20(1)	0.12(1)	0.60	870
SPS_NC	4.0(1)	0.69	0.70	92	45(8)	141(5); 68(9)	23(1)	0.15(1)	0.62	450
SPS_NC_SM	5.7(2)	0.77	0.83	88	42(2)	162(9); 92(3)	29(1)	0.19(1)	0.70	350

Figure 10 sums up the variation of M_R and H_C between powder and compacted samples; representative pictures for highly dense sample are also shown. The increase of M_R shown by the composites compared to the single SFO/SFAO phases is in line with the higher degree of exchange interaction confirmed by simulations. Consequently, the $(BH)_{MAX}$ values for NC and NC_SM are larger than that of SFAO_2 (~38 and ~96% larger, respectively). Although the absolute values are lower than the unsubstituted samples (SFO and NC_1), the magnets achieved by the design proposed in this work exhibit promising magnetic properties for rare earth-free magnets. Ideally, the large increase in coercivity due to the Al^{3+} substitution in SFO shall compensate the decrease in H_C expected in coupled composites (for comparison, H_C=300 kA/m for NC_1, see **Table S9**), which is also essential for permanent magnet applications [86]. This gap in magnetic properties between commercial ferrites and the proposed composites underscores a key challenge in the development of SPS consolidated nanocomposites. The primary challenges highlighted by this work include achieving optimal magnetic alignment during compaction, minimizing grain growth that diminishes magnetic anisotropy, and preventing the dilution of magnetic material due to the presence of non-magnetic binding phases. Addressing these issues through innovative compaction techniques, enhanced phase combinations, and improved control over microstructural evolution will be crucial steps toward narrowing the performance gap and realizing the full potential of nanoscale ferrite-based magnets.

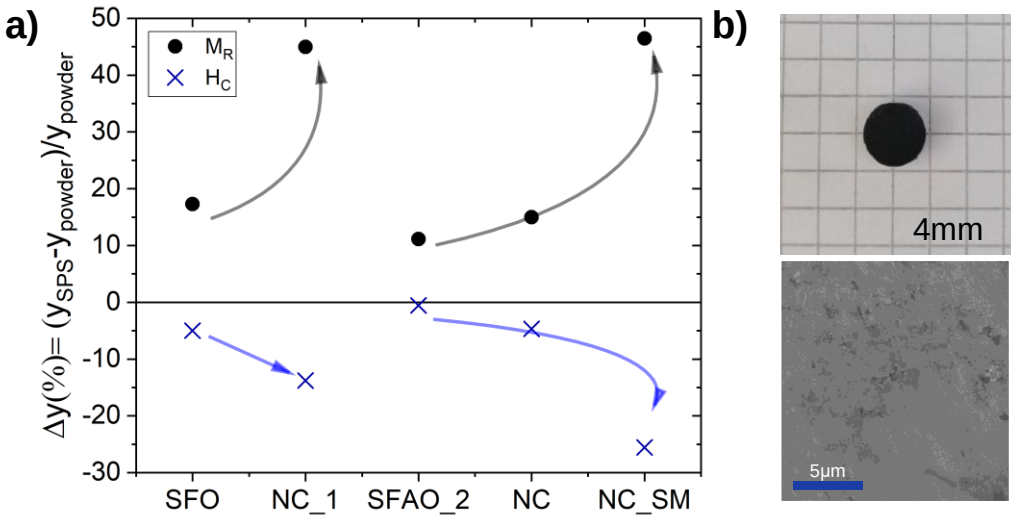

Figure 10. a) ΔM_R (%) and ΔH_C (%) between starting and SPS compacted powder samples (lines are guide to the eye). SFO and NC_1 refer to nanoscale SFO@950 and SFO/CFO 90/10 wt% nanocomposite obtained in the same conditions. b) Example of SPS pellet (SPS_NC_1) and corresponding surface image from SEM.

4. Conclusions

In this study, we have explored a bottom-up sol-gel synthesis approach to fabricate nanocomposite powders consisting of two magnetic phases, hexagonal Sr ferrite (SFO) and spinel Co ferrite (CFO), with the aim of developing a strategy for producing permanent magnets with enhanced coercivities via cost-effective and scalable methods. Through a detailed

analysis of the morphological, structural, and macroscopic magnetic properties of Al-substituted $SrFe_{12}O_{19}$ and $SrFe_{12}O_{19}/CoFe_2O_4$ nanocomposites, we have identified key factors influencing magnetic behaviour. By tuning the chemical composition of the hard phase (SFO) through Al^{3+} substitution, we achieved significant increases in magnetic coercivity while maintaining high saturation magnetization. This strategy demonstrates promise for enhancing coercivity values well beyond those of unsubstituted SFO, thus offering a pathway for tailoring magnetic properties without introducing impurity phases. Furthermore, we investigated the synthetic design of hard-soft nanocomposites, utilizing optimized SFO as the hard component and CFO as the soft component. We explored two synthesis methods, one involving preformed particles and the other involving simultaneous synthesis of both phases. Our results revealed distinct differences in cationic distribution and interface morphology between the two synthesis routes, highlighting the importance of synthetic methodology in controlling the super-exchange coupling between phases. Through epitaxial growth at the interface and careful manipulation of particle size and distribution, we achieved varying degrees of magnetic coupling, ranging from fully coupled to essentially decoupled composites. MC simulations confirm that the increase in the interface exchange coupling strength enhances the remanent magnetization of the nanocomposites, in agreement with the experimental findings. Additionally, we examined the impact of spark plasma sintering (SPS) compaction on the magnetic properties of the nanocomposites. The consolidation process resulted in increased remanent magnetization and reduced coercivity. MC results demonstrated that the SPS compaction improved particle alignment and the strong exchange coupling. It is interesting to note that the two nanophases in the nanocomposites hinder their reciprocal growth during sintering and preserve their magnetic properties. Overall, our findings demonstrate the effectiveness of the sol-gel synthesis approach in tailoring the magnetic properties of nanocomposites for advanced magnet applications.

Declaration of competing interest

The authors declare that they have no known competing financial interests or personal relationships that could have appeared to influence the work reported in this paper.

Acknowledgements

This work was supported by the Swedish Energy Agency (project number 46561-1), the Swedish Research Council (VR), and has received funding from the European Union's Horizon 2020 research and innovation program under grant agreement n°823717 – ESTEEM3 (Enabling Science and Technology through European Electron Microscopy). We acknowledge DESY (Hamburg, Germany), a member of the Helmholtz Association HGF, for the provision of experimental facilities. Parts of this research were carried out at PETRA III, beamline P02.1 within the rapid access program 2021A under proposal ID RAt-20010295, and also ID I-20221209 EC. G.E. would like to thank Dr. Alexander Schökel for assistance in using the beamline. MyFab is gratefully acknowledged for access to the cleanroom equipment by A.M. T. S. acknowledges financial support from the Swedish Research Council (VR Grant number: 2021-03675). National SPS Facility at Stockholm university is acknowledged for access to SPS. PM also thanks K G Westmans stipendiestiftelse and C.M. Lerici for travelling support. PM thanks Pedro Berastegui for the useful discussion about structural analysis and support during sample preparation for EBSD. Research conducted by S.A.I. was carried out with the financial support of the RSF (grant 22-13-00122) We also thank Dr. Marco Grotti, and Francesco Soggia from Università di Genova for ICP analysis. This work was developed in the framework of the PRIN 2022-PNRR project HyperMag (prot. P2022RRRT4) and supported by European Union – NextGenerationEU.

Author contributions

The paper and Supplementary Information were written based on the contributions of all authors. R.M., D.P. and P.M. designed the experiments; R.M. and D.P. coordinated the data analysis and discussion. P.M. synthesized the powder samples, and characterized them by XRPD, and magnetometry techniques. S.A.I. coordinated the structural discussion. G.E. carried out part of structural experiments. M.E. and P.M. prepared the SPS samples. R.M., P.M., G.V. and D.P. coordinated the magnetic measurements. G.B. and B.R. characterized the powder systems and analyzed the data by HRTEM, EDX, STEM-HAAD and EELS. B.A. contributed to the discussion of susceptibility data. N.Y. performed Mössbauer spectroscopy. A.M. characterized the SPS pellets by SEM/EDX. Monte Carlo simulations were performed by K.T. and M.V. R.M., D.P., T.S. and J.A.D.T. coordinated the discussion on magnetism. All authors contributed to the results, discussion, and revision of the article, which was written mainly by P.M. and R.M.

References

1. Gutfleisch, O., Willard, M.A., Brück, E., Chen, C.H., Sankar, S.G., and Liu, J.P. (2011) Magnetic Materials and Devices for the 21st Century: Stronger, Lighter, and More Energy Efficient. *Advanced Materials*, **23** (7), 821–842.
2. Jones, N. (2011) Materials science: The pull of stronger magnets. *Nature*, **472** (7341), 22–23.
3. Saura-Múzquiz, M., Granados-Miralles, C., Andersen, H.L., Stingaciu, M., Avdeev, M., and Christensen, M. (2018) Nanoengineered High-Performance Hexaferrite Magnets by Morphology-Induced Alignment of Tailored Nanoplatelets. *ACS Appl Nano Mater*, **1** (12), 6938–6949.
4. Stingaciu, M., Eikeland, A.Z., Gjørup, F.H., Deledda, S., and Christensen, M. (2019) Optimization of magnetic properties in fast consolidated $SrFe_{12}O_{19}$ nanocrystallites. *RSC Adv*, **9** (23), 12968–12976.
5. de Julian Fernandez, C., Sangregorio, C., de la Figuera, J., Belec, B., Makovec, D., and Quesada, A. (2021) Topical Review: Progress and Prospects of Hard Hexaferrites for Permanent Magnet Applications. *J Phys D Appl Phys*. **54** 153001.
6. Mohapatra, J., Xing, M., Elkins, J., Beatty, J., and Liu, J.P. (2021) Extraordinary Magnetic Hardening in Nanowire Assemblies: the Geometry and Proximity Effects. *Adv Funct Mater*, **31** (13), 2010157.
7. Grand View Research (2020) Permanent Magnets Market Size, Share & Trends Analysis Report By Material (Ferrite, NdFeB, Alnico, SmCo), By Application (Medical, Consumer Goods & Electronics), By Region, And Segment Forecasts, 2020 - 2027. *Grand view research, Inc. 201 Spear Street 1100, San Francisco, CA 94105, United States*.
8. Lewis, L.H., and Jiménez-Villacorta, F. (2013) Perspectives on Permanent Magnetic Materials for Energy Conversion and Power Generation. *Metallurgical and Materials Transactions A*, **44** (S1), 2–20.
9. Pullar, R.C. (2012) Hexagonal ferrites: A review of the synthesis, properties and applications of hexaferrite ceramics. *Prog Mater Sci*, **57** (7), 1191–1334.
10. Coey, J.M.D. (2011) Hard Magnetic Materials: A Perspective. *IEEE Trans Magn*, **47** (12), 4671–4681.

11. Vajtai, R. (ed.) (2013) *Springer Handbook of Nanomaterials*, Springer Berlin Heidelberg, Berlin, Heidelberg.
12. Kneller, E.F., and Hawig, R. (1991) The exchange-spring magnet: a new material principle for permanent magnets. *IEEE Trans Magn*, **27** (4), 3588–3560.
13. Cui, J., Kramer, M., Zhou, L., Liu, F., Gabay, A., Hadjipanayis, G., Balasubramanian, B., and Sellmyer, D. (2018) Current progress and future challenges in rare-earth-free permanent magnets. *Acta Mater*, **158**, 118–137.
14. Gorbachev, E.A., Trusov, L.A., Sleptsova, A.E., Kozlyakova, E.S., Alyabyeva, L.N., Yegiyan, S.R., Prokhorov, A.S., Lebedev, V.A., Roslyakov, I. V., Vasiliev, A. V., and Kazin, P.E. (2020) Hexaferrite materials displaying ultra-high coercivity and sub-terahertz ferromagnetic resonance frequencies. *Materials Today*, **32**, 13–18.
15. Han, G., Li, M., He, L., Xu, A., Chen, X., Yang, W., Liu, Y., and Yu, Y. (2023) In situ annealing achieves an ultrafast synthesis of high coercive strontium ferrite foams and beyond. *Nanoscale*, **15** (16), 7466–7471.
16. Kazin, P.E., Trusov, L.A., Zaitsev, D.D., Tretyakov, Yu.D., and Jansen, M. (2008) Formation of submicron-sized $SrFe_{12-x}Al_xO_{19}$ with very high coercivity. *J Magn Magn Mater*, **320** (6), 1068–1072.
17. Dixit, V., Nandadasa, C.N., Kim, S.-G., Kim, S., Park, J., Hong, Y.-K., Liyanage, L.S.I., and Moitra, A. (2015) Site occupancy and magnetic properties of Al-substituted M-type strontium hexaferrite. *J Appl Phys*, **117** (24).
18. Stingaciu, M., Mishra, D., de Julián Fernández, C., Cabassi, R., Eikeland, A.Z., Christensen, M., and Deledda, S. (2021) High magnetic coercive field in Ca-Al-Cr substituted strontium hexaferrite. *J Alloys Compd*, **883**, 160768.
19. Gorbachev, E.A., Kozlyakova, E.S., Alyabyeva, L.N., Ahmed, A., and Trusov, L.A. (2023) Hard ferrite magnetic insulators revealing giant coercivity and sub-terahertz natural ferromagnetic resonance at 5–300 K. *Mater Horiz*, **10** (5), 1842–1847.
20. Eikeland, A.Z., Stingaciu, M., Mamakhel, A.H., Saura-Múzquiz, M., and Christensen, M. (2018) Enhancement of magnetic properties through morphology control of $SrFe_{12}O_{19}$ nanocrystallites. *Sci Rep*, **8** (1), 7325.
21. Gorbachev, E.A., Trusov, L.A., Alyabyeva, L.N., Roslyakov, I. V., Lebedev, V.A., Kozlyakova, E.S., Magdysyuk, O. V., Sobolev, A. V., Glazkova, I.S., Beloshapkin, S.A., Gorshunov, B.P., and Kazin, P.E. (2022) High-coercivity hexaferrite ceramics featuring sub-terahertz ferromagnetic resonance. *Mater Horiz*, **9** (4), 1264–1272.
22. Belec, B., Dražić, G., Gyergyek, S., Podmiljšak, B., Goršak, T., Komelj, M., Nogués, J., and Makovec, D. (2017) Novel Ba-hexaferrite structural variations stabilized on the nanoscale as building blocks for epitaxial bi-magnetic hard/soft sandwiched maghemite/hexaferrite/maghemite nanoplatelets with out-of-plane easy axis and enhanced magnetization. *Nanoscale*, **9** (44), 17551–17560.
23. Primc, D., and Makovec, D. (2015) Composite nanoplatelets combining soft-magnetic iron oxide with hard-magnetic barium hexaferrite. *Nanoscale*, **7** (6), 2688–2697.
24. Zheng, S., Jiang, T., Wei, X., Cai, Q., Chen, C., Fang, G., and Liu, C. (2023) Achieving Multiple-Resonance Permeability at Centimeter Waveband by Joint Strategies of Hard/Soft Exchange-Coupling and Selective Doping for Superior Microwave Absorption. *The Journal of Physical Chemistry C*, **127** (3), 1704–1711.
25. Silva, L.M., Morales, M.A., Mariano, J.F.M.L., Coaquira, J.A.H., and de Araújo, J.H. (2023) Synthesis, structural and magnetic study of $BaFe_{12}O_{19}/CoFe_2O_4@CoFe_2$ nanocomposites. *J Alloys Compd*, **963**, 171285.
26. Yuan, M., Zhao, B., Yang, C., Pei, K., Wang, L., Zhang, R., You, W., Liu, X., Zhang, X., and Che, R. (2022) Remarkable Magnetic Exchange Coupling via Constructing Bi-

Magnetic Interface for Broadband Lower-Frequency Microwave Absorption. *Adv Funct Mater*, **32** (33), 2203161.
27. Shyam, P., Mørch, M., Eikeland, A.Z., Ahlburg, J., Mamakhel, A., Saura-Múzquiz, M., and Christensen, M. (2022) Combined characterization approaches to investigate magnetostructural effects in exchange-spring ferrite nanocomposite magnets. *Mater Chem Front*, **6** (17), 2422–2437.
28. Slimani, Y., Almessiere, M.A., Guner, S., Baykal, A., Sertkol, M., Alahmari, F.S., Alsulami, E.M., and Auwal, I.A. (2022) An investigation on structural, optical and magnetic properties of hard-soft $SrFe_{12}O_{19}/(CoEu_{0.02}Fe_{1.98}O_4)_x$ nanofiber composites. *J Alloys Compd*, **905**, 164240.
29. Muzzi, B., Albino, M., Innocenti, C., Petrecca, M., Cortigiani, B., Fernández, C. de J., Bertoni, G., Fernandez-Pacheco, R., Ibarra, A., Marquina, C., Ibarra, M.R., and Sangregorio, C. (2020) Unraveling the mechanism of the one-pot synthesis of exchange coupled Co-based nano-heterostructures with a high energy product. *Nanoscale*, **12** (26), 14076–14086.
30. Zeng, H., Li, J., Liu, J.P., Wang, Z.L., and Sun, S. (2002) Exchange-coupled nanocomposite magnets by nanoparticle self-assembly. *Nature*, **420** (6914), 395–398.
31. Granados-Miralles, C., Saura-Múzquiz, M., Andersen, H.L., Quesada, A., Ahlburg, J. V., Dippel, A.-C., Canévet, E., and Christensen, M. (2018) Approaching Ferrite-Based Exchange-Coupled Nanocomposites as Permanent Magnets. *ACS Appl Nano Mater*, **1** (7), 3693–3704.
32. Biesuz, M., Grasso, S., and Sglavo, V.M. (2020) What's new in ceramics sintering? A short report on the latest trends and future prospects. *Curr Opin Solid State Mater Sci*, **24** (5), 100868.
33. Kingery, W.D., Bowen, H.K., and Uhlmann, D.R. (1976) *Introduction to Ceramics*, John Wiley & Sons, Inc., New York City, New York.
34. Granados-Miralles, C., and Jenuš, P. (2021) On the potential of hard ferrite ceramics for permanent magnet technology—a review on sintering strategies. *J Phys D Appl Phys*, **54** (30), 303001.
35. El Shater, R.E., El-Ghazzawy, E.H., and El-Nimr, M.K. (2018) Study of the sintering temperature and the sintering time period effects on the structural and magnetic properties of M-type hexaferrite $BaFe_{12}O_{19}$. *J Alloys Compd*, **739**, 327–334.
36. Obi, O., Burns, L., Andalib, P., Chang, H., Chen, Y., and Harris, V.G. (2014) Improved texture of polycrystalline hexaferrites using gluconic acid dispersant. *J Appl Phys*, **115** (17).
37. Saura-Múzquiz, M., Granados-Miralles, C., Stingaciu, M., Bøjesen, E.D., Li, Q., Song, J., Dong, M., Eikeland, E., and Christensen, M. (2016) Improved performance of $SrFe_{12}O_{19}$ bulk magnets through bottom-up nanostructuring. *Nanoscale*, **8** (5), 2857–2866.
38. Rajan, A., Solaman, S.K., and Ganesanpotti, S. (2021) Cold Sintering: An Energy-Efficient Process for the Development of $SrFe_{12}O_{19}$–Li_2MoO_4 Composite-Based Wide-Bandwidth Ferrite Resonator Antenna for Ku-Band Applications. *ACS Appl Electron Mater*, **3** (5), 2297–2308.
39. Serrano, A., García-Martín, E., Granados-Miralles, C., Gorni, G., López-Sánchez, J., Ruiz-Gómez, S., Pérez, L., Quesada, A., and Fernández, J.F. (2021) Hexaferrite-based permanent magnets with upper magnetic properties by cold sintering process via a non-aqueous solvent. *Acta Mater*, **219**, 117262.
40. Palmero, E.M., Casaleiz, D., Jimenez, N.A., Rial, J., de Vicente, J., Nieto, A., Altimira, R., and Bollero, A. (2019) Magnetic-Polymer Composites for Bonding and 3D Printing of Permanent Magnets. *IEEE Trans Magn*, **55** (2), 1–4.

41. Palmero, E.M., and Bollero, A. (2021) 3D and 4D Printing of Functional and Smart Composite Materials, in *Encyclopedia of Materials: Composites*, Elsevier, pp. 402–419.
42. Bollero, A., and Palmero, E.M. (2022) Recent advances in hard ferrite magnets, in *Modern Permanent Magnets*, Elsevier, pp. 65–112.
43. Jenuš, P., Topole, M., McGuiness, P., Granados-Miralles, C., Stingaciu, M., Christensen, M., Kobe, S., and Žužek Rožman, K. (2016) Ferrite-Based Exchange-Coupled Hard-Soft Magnets Fabricated by Spark Plasma Sintering. *Journal of the American Ceramic Society*, **99** (6), 1927–1934.
44. Jenuš, P., Učakar, A., Repše, S., Sangregorio, C., Petrecca, M., Albino, M., Cabassi, R., de Julián Fernández, C., and Belec, B. (2021) Magnetic performance of $SrFe_{12}O_{19}$–$Zn_{0.2}Fe_{2.8}O_4$ hybrid magnets prepared by spark plasma sintering. *J Phys D Appl Phys*, **54** (20), 204002.
45. Maltoni, P., Barucca, G., Rutkowski, B., Spadaro, M.C., Jönsson, P.E., Varvaro, G., Yaacoub, N., De Toro, J.A., Peddis, D., and Mathieu, R. (2024) Unraveling Exchange Coupling in Ferrites Nano-Heterostructures. *Small*. **20**, 2304152.
46. Maltoni, P., Sarkar, T., Barucca, G., Varvaro, G., Locardi, F., Peddis, D., and Mathieu, R. (2021) Tuning the Magnetic Properties of Hard–Soft $SrFe_{12}O_{19}$/$CoFe_2O_4$ Nanostructures via Composition/Interphase Coupling. *The Journal of Physical Chemistry C*, **125** (10), 5927–5936.
47. Maltoni, P., Baričić, M., Barucca, G., Spadaro, M.C., Arbiol, J., Yaacoub, N., Peddis, D., and Mathieu, R. (2023) Tunable particle-agglomeration and magnetic coupling in bi-magnetic nanocomposites. *Physical Chemistry Chemical Physics*. **25**, 27817-27828
48. Baričić, M., Maltoni, P., Barucca, G., Yaacoub, N., Omelyanchik, A., Canepa, F., Mathieu, R., and Peddis, D. (2024) Chemical engineering of cationic distribution in spinel ferrite nanoparticles: the effect on the magnetic properties. *Physical Chemistry Chemical Physics*, **26** (7), 6325–6334.
49. Normile, P.S., Andersson, M.S., Mathieu, R., Lee, S.S., Singh, G., and De Toro, J.A. (2016) Demagnetization effects in dense nanoparticle assemblies. *Appl Phys Lett*, **109** (15), 152404.
50. Coey, J.M.D. (2001) *Magnetism and Magnetic Materials*, Cambridge University Press.
51. Bernal, S., Botana, F.J., Calvino, J.J., López-Cartes, C., Pérez-Omil, J.A., and Rodríguez-Izquierdo, J.M. (1998) The interpretation of HREM images of supported metal catalysts using image simulation: profile view images. *Ultramicroscopy*, **72** (3–4), 135–164.
52. Rietveld, H.M. (1969) A profile refinement method for nuclear and magnetic structures. *J Appl Crystallogr*, **2** (2), 65–71.
53. Rodríguez-Carvajal, J. (1993) Recent advances in magnetic structure determination by neutron powder diffraction. *Physica B Condens Matter*, **192** (1–2), 55–69.
54. Trohidou, K., and Vasilakaki, M. (2011) Monte Carlo Studies of Magnetic Nanoparticles, in *Applications of Monte Carlo Method in Science and Engineering*, InTech. doi: 10.5772/15930.
55. Vasilakaki, M., Gemenetzi, F., Devlin, E., Yi, D.K., Riduan, S.N., Lee, S.S., Ying, J.Y., Papaefthymiou, G.C., and Trohidou, K.N. (2021) Size effects on the magnetic behavior of γ-Fe_2O_3 core/SiO_2 shell nanoparticle assemblies. *J Magn Magn Mater*, **522**, 167570.
56. Trusov, L.A., Gorbachev, E.A., Lebedev, V.A., Sleptsova, A.E., Roslyakov, I. V., Kozlyakova, E.S., Vasiliev, A. V., Dinnebier, R.E., Jansen, M., and Kazin, P.E. (2018) Ca–Al double-substituted strontium hexaferrites with giant coercivity. *Chemical Communications*, **54** (5), 479–482.

57. Sandiumenge, F., Gali, S., and Rodriguez, J. (1988) X-ray profile analysis of cation distribution in $SrAl_xFe_{12-x}O_{19}$ solid solution. *Mater Res Bull*, **23** (5), 685–692.
58. Maltoni, P., Sarkar, T., Varvaro, G., Barucca, G., Ivanov, S.A., Peddis, D., and Mathieu, R. (2021) Towards bi-magnetic nanocomposites as permanent magnets through the optimization of the synthesis and magnetic properties of $SrFe_{12}O_{19}$ nanocrystallites. *J Phys D Appl Phys*, **54** (12), 124004.
59. Saura-Múzquiz, M., Eikeland, A.Z., Stingaciu, M., Andersen, H.L., Granados-Miralles, C., Avdeev, M., Luzin, V., and Christensen, M. (2020) Elucidating the relationship between nanoparticle morphology, nuclear/magnetic texture and magnetic performance of sintered $SrFe_{12}O_{19}$ magnets. *Nanoscale*, **12** (17), 9481–9494.
60. Bernal, S., Botana, F.J., Calvino, J.J., López, C., Pérez-Omil, J.A., and Rodríguez-Izquierdo, J.M. (1996) High-resolution electron microscopy investigation of metal–support interactions in Rh/TiO_2. *J. Chem. Soc., Faraday Trans.*, **92** (15), 2799–2809.
61. Momma, K., and Izumi, F. (2008) VESTA : a three-dimensional visualization system for electronic and structural analysis. *J Appl Crystallogr*, **41** (3), 653–658.
62. Stoner, E.C., and Wohlfarth, E.P. (1948) A mechanism of magnetic hysteresis in heterogeneous alloys. *Philosophical Transactions of the Royal Society of London. Series A, Mathematical and Physical Sciences*, **240** (826), 599–642.
63. Stingaciu, M., Mishra, D., de Julián Fernández, C., Cabassi, R., Eikeland, A.Z., Christensen, M., and Deledda, S. (2021) High magnetic coercive field in Ca-Al-Cr substituted strontium hexaferrite. *J Alloys Compd*, **883**, 160768.
64. Gorbachev, E.A., Lebedev, V.A., Kozlyakova, E.S., Alyabyeva, L.N., Ahmed, A., Cervellino, A., and Trusov, L.A. (2023) Tuning the microstructure, magnetostatic and magnetodynamic properties of highly Al-substituted M-type Sr/Ca hexaferrites prepared by citrate-nitrate auto-combustion method. *Ceram Int*. **49** (16), 26411-26419.
65. Abo, G.S., Hong, Y.-K., Jalli, J., Lee, J.-J., Park, J.-H., Bae, S., Kim, S.-G., Choi, B.-C., and Tanaka, T. (2012) Shape Dependent Coercivity Simulation of a Spherical Barium Ferrite (S-BaFe) Particle with Uniaxial Anisotropy. *Journal of Magnetics*, **17** (1), 1–5.
66. Dahal, J.N., Wang, L., Mishra, S.R., Nguyen, V.V., and Liu, J.P. (2014) Synthesis and magnetic properties of $SrFe_{12-x-y}Al_xCo_yO_{19}$ nanocomposites prepared via autocombustion technique. *J Alloys Compd*, **595**, 213–220.
67. Sláma, J., Šoka, M., Grusková, A., Gonzalez, A., and Jančárik, V. (2011) Hopkinson Effect Study in Spinel and Hexagonal Ferrites. *Journal of Electrical Engineering*, **62** (4), 239–243.
68. Pfeiffer, H., and Schüppel, W. (1994) Temperature dependence of the magnetization in fine particle systems and the Hopkinson effect. Application to barium ferrite powders. *J Magn Magn Mater*, **130** (1–3), 92–98.
69. Dunlop, D.J. (2014) High-temperature susceptibility of magnetite: a new pseudo-single-domain effect. *Geophys J Int*, **199** (2), 707–716.
70. Muralidhar, S., Gräfe, J., Chen, Y.-C., Etter, M., Gregori, G., Ener, S., Sawatzki, S., Hono, K., Gutfleisch, O., Kronmüller, H., Schütz, G., and Goering, E.J. (2017) Temperature-dependent first-order reversal curve measurements on unusually hard magnetic low-temperature phase of MnBi. *Phys Rev B*, **95** (2), 024413.
71. Kittel, C. (1949) Physical Theory of Ferromagnetic Domains. *Rev Mod Phys*, **21** (4), 541–583.
72. Hubert, A., and Schäfer, R. (1998) *Magnetic Domains*, Springer Berlin Heidelberg, Berlin, Heidelberg.
73. Muscas, G., Yaacoub, N., Concas, G., Sayed, F., Sayed Hassan, R., Greneche, J.M., Cannas, C., Musinu, A., Foglietti, V., Casciardi, S., Sangregorio, C., and Peddis, D.

(2015) Evolution of the magnetic structure with chemical composition in spinel iron oxide nanoparticles. *Nanoscale*, **7** (32), 13576–13585.
74. Givord, D., Rossignol, M., and Barthem, V.M.T.S. (2003) The physics of coercivity. *J Magn Magn Mater*, **258–259**, 1–5.
75. Anantharamaiah, P.N., and Joy, P.A. (2015) Magnetic and magnetostrictive properties of aluminium substituted cobalt ferrite synthesized by citrate-gel method. *J Mater Sci*, **50** (19), 6510–6517.
76. Sharifianjazi, F., Moradi, M., Parvin, N., Nemati, A., Jafari Rad, A., Sheysi, N., Abouchenari, A., Mohammadi, A., Karbasi, S., Ahmadi, Z., Esmaeilkhanian, A., Irani, M., Pakseresht, A., Sahmani, S., and Shahedi Asl, M. (2020) Magnetic $CoFe_2O_4$ nanoparticles doped with metal ions: A review. *Ceram Int*, **46** (11), 18391–18412.
77. Shannon, R.D. (1976) Revised effective ionic radii and systematic studies of interatomic distances in halides and chalcogenides. *Acta Crystallographica Section A*, **32** (5), 751–767.
78. Kneller, E.F., and Hawig, R. (1991) The exchange-spring magnet: a new material principle for permanent magnets. *IEEE Trans Magn*, **27** (4), 3588–3560.
79. Belec, B., Dražić, G., Gyergyek, S., Podmiljšak, B., Goršak, T., Komelj, M., Nogués, J., and Makovec, D. (2017) Novel Ba-hexaferrite structural variations stabilized on the nanoscale as building blocks for epitaxial bi-magnetic hard/soft sandwiched maghemite/hexaferrite/maghemite nanoplatelets with out-of-plane easy axis and enhanced magnetization. *Nanoscale*, **9** (44), 17551–17560.
80. Quesada, A., Granados-Miralles, C., López-Ortega, A., Erokhin, S., Lottini, E., Pedrosa, J., Bollero, A., Aragón, A.M., Rubio-Marcos, F., Stingaciu, M., Bertoni, G., de Julián Fernández, C., Sangregorio, C., Fernández, J.F., Berkov, D., and Christensen, M. (2016) Energy Product Enhancement in Imperfectly Exchange-Coupled Nanocomposite Magnets. *Adv Electron Mater*, **2** (4), 1500365.
81. Stearns, M.B., and Cheng, Y. (1994) Determination of para- and ferromagnetic components of magnetization and magnetoresistance of granular Co/Ag films (invited). *J Appl Phys*, **75** (10), 6894–6899.
82. Antón, R., González, J., Andrés, J., Normile, P., Canales-Vázquez, J., Muñiz, P., Riveiro, J., and De Toro, J. (2017) Exchange Bias Optimization by Controlled Oxidation of Cobalt Nanoparticle Films Prepared by Sputter Gas Aggregation. *Nanomaterials*, **7** (3), 61.
83. Leijon, J., Sjölund, J., Ekergård, B., Boström, C., Eriksson, S., Temiz, I., and Leijon, M. (2017) Study of an Altered Magnetic Circuit of a Permanent Magnet Linear Generator for Wave Power. *Energies (Basel)*, **11** (1), 84.
84. Grades of Ferrite.
85. Gjørup, F.H., Saura-Múzquiz, M., Ahlburg, J.V., Andersen, H.L., and Christensen, M. (2018) Coercivity enhancement of strontium hexaferrite nano-crystallites through morphology controlled annealing. *Materialia (Oxf)*, **4**, 203–210.
86. Eriksson, S., and Eklund, P. (2021) Effect of magnetic properties on performance of electrical machines with ferrite magnets. *J Phys D Appl Phys*, **54** (5), 054001.